ORIGINAL RESEARCH

The Institution of Engineering and Technology WILEY

Modified magnetic equivalent circuit model for magnetic field analysis of one cage-rotor induction motor used in electric submersible pumps

Farhad Rezaee-Alam[1] | Abbas Nazari Marashi[2] | Sam Roozbehani[2]

[1]Department of Electrical Engineering, Lorestan University, Khorramabad, Iran

[2]Electrical Machine Research Group, ACECR, Khajeh Nasir Toosi University of Technology Branch, Tehran, Iran

Correspondence

Sam Roozbehani, Shariati Street, Seyed Khandan Bridge, Tehran, Iran.
Email: samroozbehani@acecr.ac.ir

Abstract

Here, a modified magnetic equivalent circuit model which can accurately consider the air-gap region is presented. The main defect of magnetic equivalent circuit model is in the modelling of air-gap region. To solve this problem, a new approach based on conformal mappings is presented to accurately calculate the air-gap permeances between the elements of stator and rotor while considering the real paths of flux tubes in air gap. The distributions of equivalent virtual currents on the both sides of air gap are obtained through modified magnetic equivalent circuit model, which represent the effects of slots, magneto motive force drops in iron parts, and magneto motive force sources. The conformal mapping method is then used to calculate the components of air-gap magnetic field for every operating point under starting conditions and different loads. One typical cage-rotor induction motor, which is used in electric submersible pumps, is considered to investigate the accuracy of modified magnetic equivalent circuit model. Some of the analytical results obtained through modified magnetic equivalent circuit model are verified by comparing with the corresponding results obtained from finite element method and experiment set up.

1 | INTRODUCTION

Magnetic equivalent circuit (MEC) model is an accurate technique for electromagnetic modelling of electric machines [1]. The main property of MEC model is to consider the magnetic saturation in iron parts. Other analytical techniques such as winding function theory [2], sub-domain model [3], conformal mapping (CM) method [4], and field reconstruction method [5] cannot consider the magnetic saturation.

MEC model acts based on solving a permeance network including the magneto motive force (MMF) sources which represent the effect of windings and permanent magnets (PMs) [6]. The accuracy of MEC model depends on the number of nodes or branches in the permeance network. A simple MEC model has been used to model and analyse the cage rotor

induction motors (CRIMs) [1, 7, 8] while using the Stovic's method [6] to calculate the air-gap permeances.

For accurate modelling of the air-gap region, a MEC model was introduced in ref. [9], which helps from the solution of Maxwell's equation in air gap. One hybrid analytical model (HAM) based on models of MEC and subdomain has been also presented in ref. [10, 11], which considers the iron parts by MEC model and other regions through sub-domain model. A novel mesh-based reluctance network was introduced in ref. [12] for precise modelling the air-gap region. Multi-slice MEC model was used to quasi-3D model of one outer-rotor single-phase induction motor while considering the skewing effect of rotor slots [13]. In many HAMs based on CM method [14–17] and winding function theory [18–20], MEC model has been used to accurately consider the iron parts.

In this paper, a modified magnetic equivalent circuit (MMEC) model is introduced for accurate modelling of the CRIMs used in electric submersible pumps (ESPs), which can accurately consider the air-gap region through permeances obtained through CMs. This paper is organised as follows:

The studied electric machines are introduced in Section 2. The proposed MMEC model is introduced in Section 3. The dynamic results and magnetic field analysis obtained through MMEC model are presented in Section 4. The conclusions are presented in Section 5.

2 | ANALYSED CRIM

The CRIMs used in ESPs are filled with a highly refined mineral oil that provides dielectric strength, lubrication of bearings and good thermal conductivity. Therefore, the stator and rotor slots of CRIM used in ESPs should be closed, as shown in zoomed view in Figure 1b. The main parameters of

analysed CRIM are introduced in Table 1. The winding layout of stator is single-layer concentrated winding (Figure 1a).

CRIMs used in ESP have small diameter to fit inside an oil well. For this reason, the rated horsepower necessitates designing a very long motor [21]. As shown in Table 1, the ratio of axial length per diameter is about 43. Under this condition, the rotor could be made in one piece but because of the high rotational speeds and their extreme slenderness, the rotor would be extremely unstable radially. This is why the ESP motors are manufactured with rotors made of short segments with radial bearings between them to stabilise the operation of shaft [22]. For analysed CRIM in this paper, a concatenated multi-rotor design (nine stages) with bearing between adjacent rotors is installed inside the stator lamination stack (Figure 2) so that the magnetic coupling between nine stages is negligible.

For electromagnetic analysis, a CRIM with one rotor and one stator with an axial length equal to 600 mm, and the rated line to line voltage equal to $\frac{2345}{9}(V - \text{RMS})$ is considered. Other parameters are considered similar to real CRIM.

3 | MMEC MODEL

In MMEC model presented in this paper, the stator and rotor are respectively divided into 630 and 768 elements in cylindrical coordinate system. 8640 permeances are considered between the elements of stator and rotor in air gap. Figure 3 shows a zoomed view of MMEC model. This paper presents a new approach to calculate the air-gap permeances, accurately.

3.1 | Calculation of permeances

Figure 4 shows two typical elements of stator and rotor on both sides of air gap. The air-gap permeance between the ith
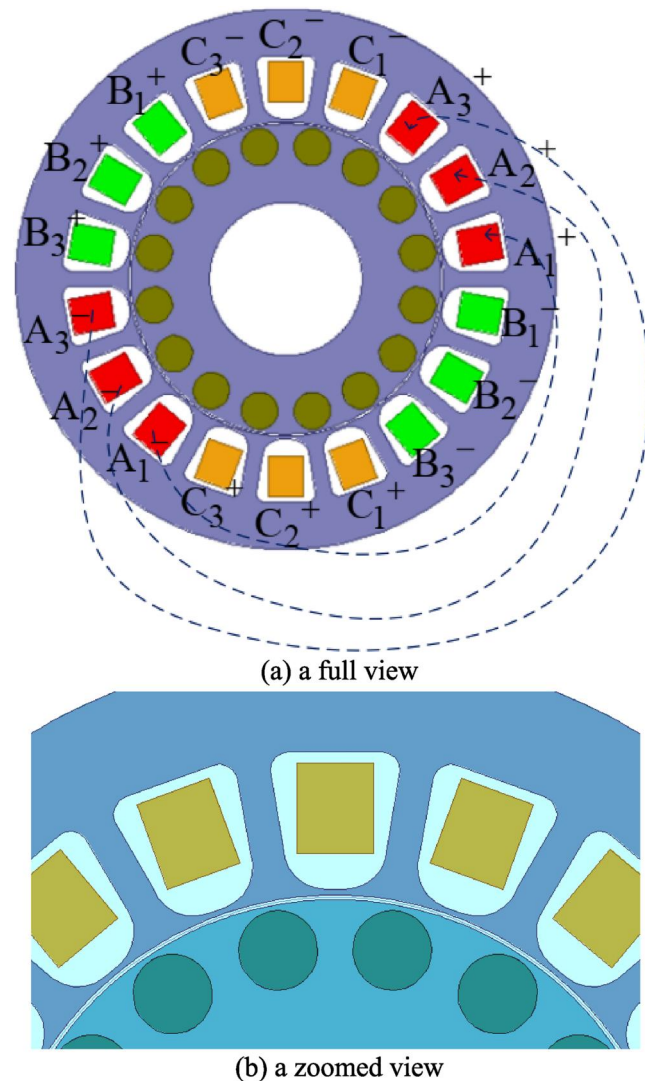

(a) a full view

(b) a zoomed view

FIGURE 1 Analysed cage rotor induction motor.

TABLE 1 Main parameters of analysed cage rotor induction motor.

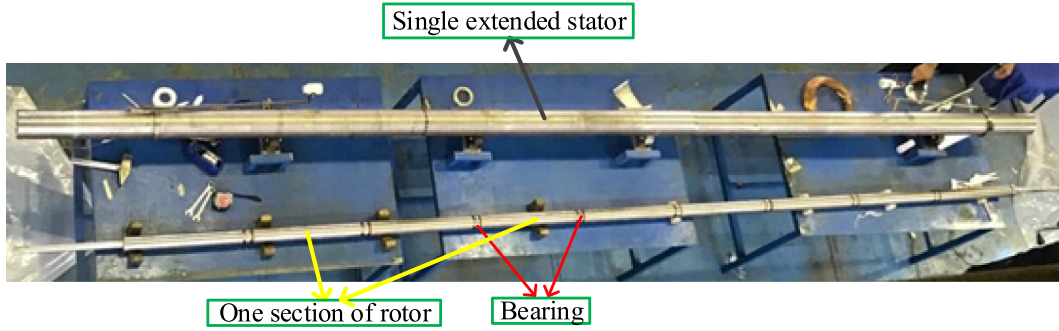| Parameter	Value and unit
Number of pole pairs, p	1
Number of stator slots, Q_s	18
Number of stator slots, Q_r	16
Rated power, P	130 hp
Rated line-line voltage, V	2345 V
Rated frequency, f	50 Hz
Rated rotor speed, n_r	2845 rpm
Axial length, L	5.4 m
Air-gap length, g	0.5 mm
Stator inner diameter	71 mm
Stator winding type	Concentrated
Winding turns per coil, N_c	12

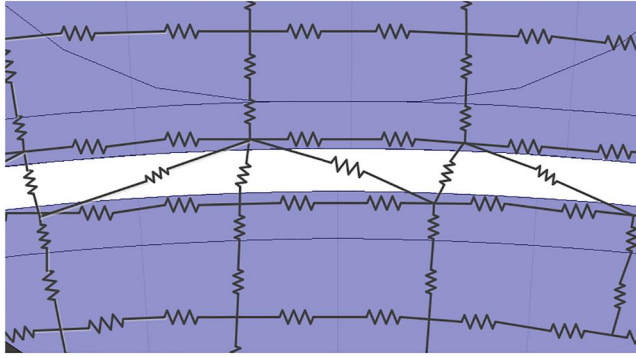**FIGURE 2**   Structure of cage rotor induction motor.

FIGURE 3   A zoomed view of modified magnetic equivalent circuitMMEC model.

FIGURE 4   One typical air-gap permeance.

element of stator and jth element of rotor is conventionally calculated as follows [6]:

$$G_{i,j}(\gamma)$$
$$= \begin{cases} G_{max} & 0 \leq \gamma \leq \gamma_2 \quad \text{and} \\ & (2\pi - \gamma_2) \leq \gamma \leq (2\pi) \\ \dfrac{G_{max}}{2} \times \left(1 + \cos\left(\dfrac{\pi(\gamma - \gamma_2)}{\gamma_1 - \gamma_2}\right)\right) & \gamma_2 \leq \gamma \leq \gamma_1 \\ \dfrac{G_{max}}{2} \times \left(1 + \cos\left(\dfrac{\pi(\gamma - 2\pi + \gamma_2)}{\gamma_1 - \gamma_2}\right)\right) & (2\pi - \gamma_1) \leq \gamma \leq (2\pi - \gamma_2) \\ 0 & \gamma_1 \leq \gamma \leq (2\pi - \gamma_1) \end{cases}$$
$$(1)$$

where $\gamma_2 = \frac{|W_s - W_r|}{D_g}$, $\gamma_1 = \frac{|W_s + W_r|}{D_g}$, W_s and W_r are, respectively, the width of stator and rotor elements, and D_g is the average diameter of air gap.

Formula (1) is known as the Stovic's method, which cannot consider the real paths of air-gap flux tubes. For this reason, a new approach based on CMs is presented which can accurately consider the air-gap region without any complex calculations. To this end, two virtual coils with one turn are considered on the ith element of stator and jth element of rotor (Figure 4).
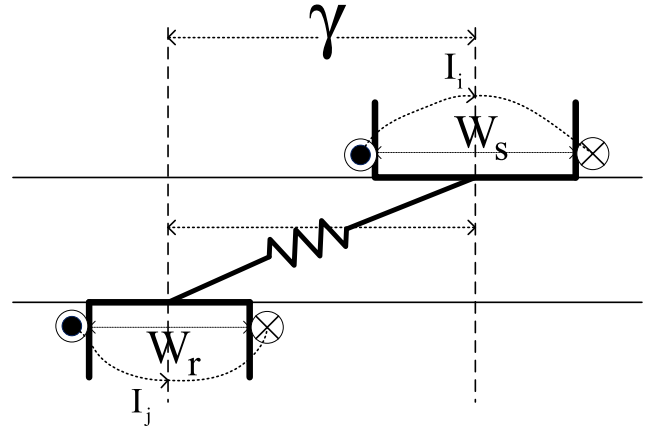
The mutual inductance between virtual coils is then calculated by using CM method [23] as follows:

$$\begin{cases} G_{i,j}(\gamma) = L_{i,j}(\gamma) = \dfrac{\lambda_i(\gamma)}{I_j} \bigg| I_i = 0 \\ \lambda_i(\gamma) = R_g \times L \times \displaystyle\int_0^{2\pi} n_i(\varphi) \times B_{r,j}(\varphi, \gamma) d\varphi \end{cases} \quad (2)$$

where λ_i is the flux-linkage with ith virtual coil on the inner surface of stator, I_j is the magnitude of current in jth virtual coil on the rotor surface, R_g is the radius of contour in the middle of air gap, L is the axial length of core, φ is the angular position on the contour, $n_i(\varphi)$ is the turn function of ith virtual coil on the inner surface of stator and $B_{r,j}(\varphi)$ is the radial component of air-gap magnetic flux density due to excitation of jth virtual coil on the rotor surface.

Figure 5a shows the physical slotless air gap which is including two equivalent line currents in the position of jth virtual coil as follows:

$$\begin{cases} I_1 = I_j @ (r_1, \theta_1), \Delta\theta_1 = \theta - \theta_1 \\ I_2 = -I_j @ (r_2, \theta_2), \Delta\theta_2 = \theta - \theta_2 \end{cases} \quad (3)$$
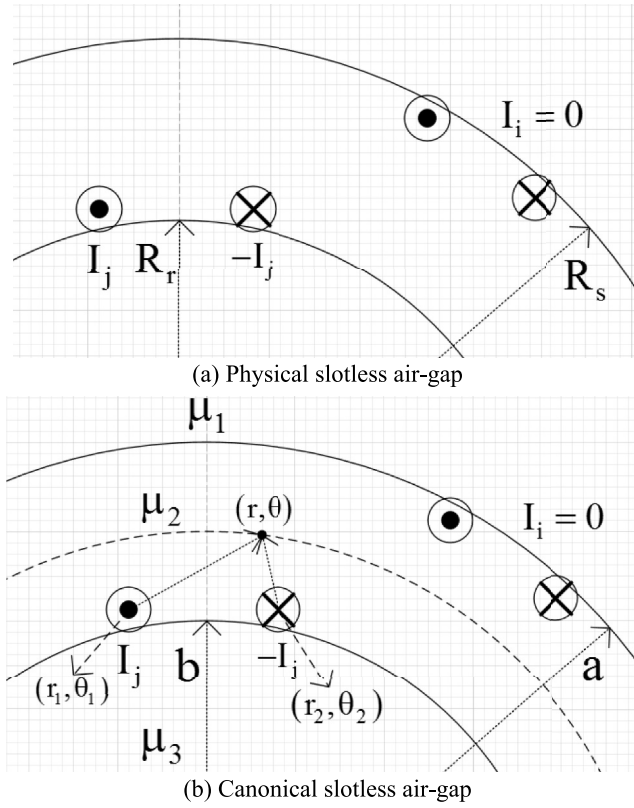
(a) Physical slotless air-gap

(b) Canonical slotless air-gap

FIGURE 5 Slotless air gap.

To calculate the radial component of flux density in the middle of air gap $(B_{r,j}(\varphi))$, the physical slotless air gap should be mapped into the canonical slotless air gap with the average radius of 1 m by using the following CM:

$$T = \frac{2}{R_s + R_r} \quad (4)$$

where R_s and R_r are the inner radius of stator and outer radius of rotor, respectively.

Figure 5b shows a zoomed view of canonical slotless air gap including the equivalent line currents of virtual coils. Hague's solution necessitates the average radius of 1 m for canonical slotless air gap so that

$$b < 1 < a \quad (5)$$

Hague's solution [24, 25] is used to calculate the scalar magnetic potential in canonical domain due to jth virtual coil as shown in Equation (6). The air-gap flux density due to jth virtual coil in canonical and physical slotless air gaps is then calculated as shown in Equations (7)–(11). Formula (7) is a famous mathematical principle in electromagnetics, which is used to calculate the components of air-gap magnetic flux density while having the distribution of scalar magnetic potential.

$$\psi(r,\theta) = \sum_{k=1}^{2}\left[\frac{I_k \times \Delta\theta_k}{2\pi} + \sum_{n=1}^{\infty}\left(A_{n,k} \times r^n + \left(\frac{I_k \times r_k{}^n}{2n\pi} + B_{n,k}\right)r^{-n}\right)\sin(n \times \Delta\theta_k)\right] \quad (6)$$

$$B_c(r,\theta) = B_{r-c}\overrightarrow{a_r} + B_{t-c}\overrightarrow{a_t} = -\mu_0 \times \overrightarrow{\nabla\psi(r,\theta)} = -\mu_0 \times \left[\frac{d\psi(r,\theta)}{dr}\overrightarrow{a_r} + \frac{1}{r}\frac{d\psi(r,\theta)}{d\theta}\overrightarrow{a_t}\right] \quad (7)$$

$$B_{r-c}(r,\theta) = -\frac{1}{r}\sum_{k=1}^{2}\sum_{n=1}^{\infty}\left[n \times A_{n,k} \times r^n - \left(\frac{I_k \times r_k{}^n}{2\pi} + n \times B_{n,k}\right)r^{-n}\right]\sin(n \times \Delta\theta_k) \quad (8)$$

$$B_{t-c}(r,\theta) = -\mu_0\sum_{k=1}^{2}\left[\frac{I_k}{2\pi} + \frac{1}{r}\sum_{n=1}^{\infty}\left(n \times A_{n,k} \times r^n + \left(\frac{I_k \times r_k{}^n}{2\pi} + n \times B_{n,k}\right)r^{-n}\right)\cos(n \times \Delta\theta_k)\right] \quad (9)$$

$$\begin{cases} A_{n,k} = \dfrac{-I_k(\mu_1 - \mu_2)\left[b^{2n}(\mu_3 - \mu_2) + r_k{}^{2n}(\mu_3 + \mu_2)\right]}{r_k{}^n \times (2n\pi) \times \left[b^{2n}(\mu_2 - \mu_3)(\mu_1 - \mu_2) + a^{2n}(\mu_2 + \mu_3)(\mu_1 + \mu_2)\right]} \\[2em] B_{n,k} = \dfrac{b^{2n} \times I_k \times (\mu_3 - \mu_2)[r_k{}^{2n} \times (\mu_1 - \mu_2) + a^{2n}(\mu_1 + \mu_2)]}{r_k{}^n \times (2n\pi) \times \left[b^{2n}(\mu_2 - \mu_3)(\mu_1 - \mu_2) + a^{2n}(\mu_2 + \mu_3)(\mu_1 + \mu_2)\right]} \end{cases} \quad (10)$$

$$B(r,\theta) = T \times B_c(r,\theta) = B_r\overrightarrow{a_r} + B_t\dot{a_t}. \quad (11)$$

Equations (8) and (9) show the closed form of radial and tangential components of air-gap flux density in canonical slotless air gap. Equation (11) is used to map the result of air-gap magnetic field in slotless canonical domain into the slotless physical domain. For a typical rotor position, Figure 6 shows the radial component of air-gap flux density while considering $I_j = 1(A)$ and $I_i = 0(A)$.

The mutual air-gap permeance between ith element of stator and jth element of rotor is then calculated using Equation (2) while considering the rotation of rotor. As shown in Figure 7, the real paths of air-gap flux tubes such as concentration in low reluctance region, and fringing in high reluctance region, is considered by proposed technique better than the Stovic's method. By the classic method, all air-gap flux tubes are assumed in radial direction in overlapping region of elements on both sides of air gap. From the point of view of CM method, this assumption is not acceptable and the real paths of air-gap flux tubes are considered. For this reason, the peak value of $G_{i,j}(\gamma)$ obtained through CM method is less than it obtained from the classic method. With the rotation of rotor and reducing in area of overlapping region, the fringing (expansion) of air-gap flux tubes are better modelled by using the CM method.

By using the curve fitting toolbox (MATLAB), Gaussian function can be used to extract an accurate mathematic formula for $G_{i,j}(\gamma)$ as follows:
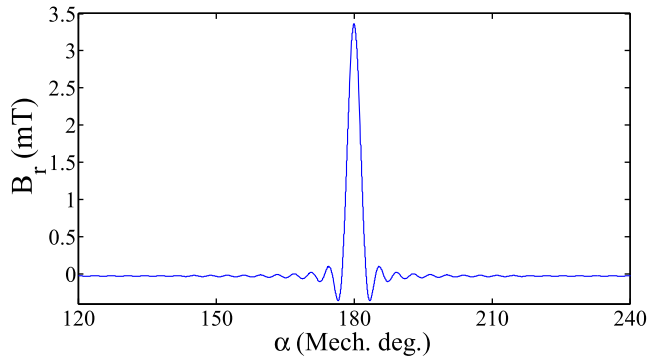
$$G_{i,j}(\gamma) = \sum_{i=1}^{5} a_i \times e^{-\left(\frac{\gamma - b_i}{c_i}\right)^2} \tag{12}$$

$a = [-0.3556, 29.52, 0, 6.699, 6.616];$
$b = [3.145, 3.14, 13.14, 3.181, 3.1];$
$c = [23.68, 0.0333, 2.394 \times 10^{-4}, 0.0205, 0.0204];$
$G_{i+1,j}(\gamma) = G_{i,j}(\gamma - W_s);$
$G_{i,j+1}(\gamma) = G_{i,j}(\gamma + W_r)$

Figure 8 shows the MEC for each element of stator and rotor in cylindrical coordinate. The radial and tangential components of permeance (G_r and G_t) are calculated as follows:

$$\begin{cases} G_r = \dfrac{2 \times \mu_0 \times \mu_r \times \beta \times L}{\ln\left(\dfrac{r_2}{r_1}\right)} \\[6mm] G_t = \dfrac{2 \times \mu_0 \times \mu_r \times L \times \ln\left(\dfrac{r_2}{r_1}\right)}{\beta} \end{cases} \tag{13}$$

3.2 | Equation system of MMEC model

After obtaining the permeances of elements in magnetic and non-magnetic regions, the system of algebraic equations including magnetic and electric equations is defined as shown in Equations (14) and (15):

$$\begin{bmatrix} \lambda_s \\ \lambda_r \end{bmatrix} = \int \left(\begin{bmatrix} V_s \\ 0 \end{bmatrix} - \begin{bmatrix} R_s & 0 \\ 0 & R_r \end{bmatrix} \begin{bmatrix} I_s \\ I_r \end{bmatrix} \right) dt \tag{14}$$

$$A(X)X = B \tag{15}$$

FIGURE 6 Radial component of air-gap flux density.
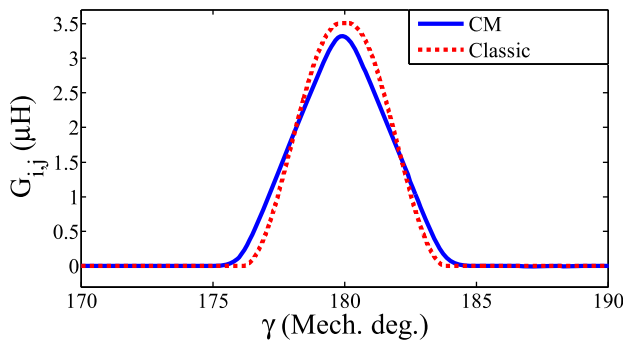
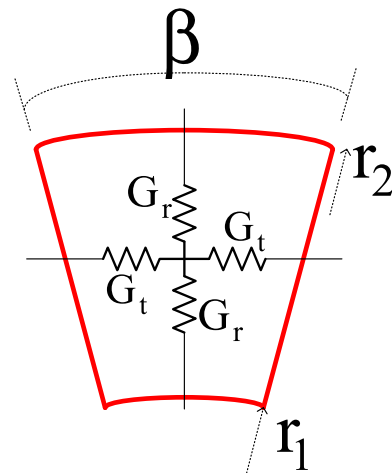

FIGURE 7 Air-gap permeance.

FIGURE 8 One typical element in modified magnetic equivalent circuit model.

$$\begin{bmatrix} [A_{n-n}]_{N \times N} & [A_{n-s}]_{N \times 3} & [A_{n-r}]_{N \times 17} \\ [A_{s-n}]_{3 \times N} & [A_{s-s}]_{3 \times 3} & [A_{s-r}]_{3 \times 17} \\ [A_{r-n}]_{17 \times N} & [A_{r-s}]_{17 \times 3} & [A_{r-r}]_{17 \times 17} \end{bmatrix} \begin{bmatrix} [U]_{N \times 1} \\ [I_s]_{3 \times 1} \\ [I_r]_{17 \times 1} \end{bmatrix}$$
$$= \begin{bmatrix} [0]_{N \times 1} \\ [\lambda_s]_{3 \times 1} \\ [\lambda_r]_{17 \times 1} \end{bmatrix}. \tag{16}$$

Formula (15) is expanded in Equation (16).

In Equation (16), 'N' is the number of node in permeance network $([A_{n-n}]_{N \times N})$, index 's' and 'r' represent the stator and rotor, other elements in $A(X)$ are the connection matrix, $[U]_{N \times 1}$ is the scalar magnetic potential matrix of nodes, $[I_s]_{3 \times 1}$ is the matrix of stator currents, $[I_r]_{17 \times 1}$ is the matrix of rotor currents, $[\lambda_s]_{3 \times 1}$ is flux-linkage matrix of stator phases, and $[\lambda_r]_{17 \times 1}$ is flux-linkage matrix of rotor loops.

Figure 9 shows the B–H curve of ferromagnetic material used in stator and rotor cores. To calculate the non-linear permeances in $A(X)$, the relative permeability (μ_r) in Equation (13) should be calculated as follows:

$$\mu_r = \frac{dB}{dH} = f(H) = f\left(\frac{\Delta u}{l}\right) \tag{17}$$

where Δu is the scalar magnetic potential across the permeance element, and l is the length of permeance element.

The Newton–Raphson algorithm is most popular algorithm to solve the non-linear problem in electromagnetics. In order to apply the Newton–Raphson algorithm, the non-linear matrix equation should be written as follows:

$$g(X) = A(X)X - B = 0. \tag{18}$$

By using the Newton–Raphson algorithm, the non-linear matrix Equations (14) and (15) is reduced to a system of linear equations in iteration form as follows:

$$J^k \Delta X^k = -g\left(X^k\right)$$
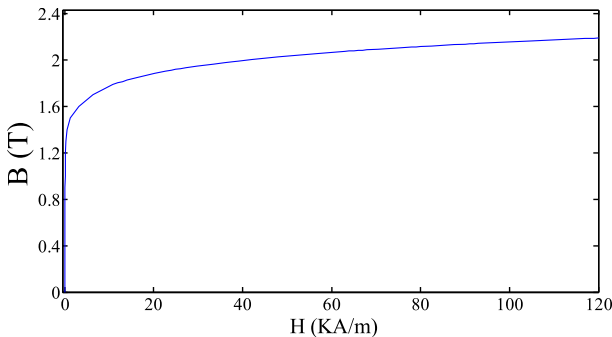$$\Delta X^k = X^{k+1} - X^k \tag{19}$$

FIGURE 9 B–H curve of core.

where ΔX^k and J^k are, respectively, the incremental vector and Jacobian matrix in kth iteration [26].

Electromagnetic torque is calculated for every operating point as follows:

$$T_e(\gamma) = 9 \times \sum_{i=1}^{90} \sum_{j=1}^{96} \left[U_i - U_j\right]^2 \times \frac{dG_{i,j}}{d\gamma}. \tag{20}$$

The mechanical equations are then solved using finite difference method as follows:

$$\begin{cases} T_e(\gamma) - T_L = J\dfrac{d\omega_r}{d\gamma} + D\omega_r \\ \omega_r = \dfrac{d\gamma}{dt} \end{cases}$$

$$\begin{cases} \omega_r(k+1) = \left[1 - \dfrac{D \times \Delta t}{J}\right]\omega_r(k) + \dfrac{\Delta t}{J}\left[T_e(k) - T_L\right] \\ \gamma(k+1) = \gamma(k) + \Delta t \times \omega_r(k) \end{cases} \tag{21}$$

where T_L is the load torque, J is the moment inertia of rotor and shaft, D is the damping coefficient and $\gamma(k)$ is the rotor position in kth step of simulation.

4 | RESULTS AND DISCUSSION

4.1 | Dynamic results

A rated three-phase voltage source is applied to the stator winding with star connection while considering a squirrel cage for rotor bars. Figure 10 shows the stator phase current under different loading conditions. As the load increases, the harmonic content of stator phase current is intensified due to the simultaneous effect of magnetic saturation, slotting effect, and winding distribution. Figure 11 shows the starting of analysed CRIM under no-load condition. The results of electromagnetic torque obtained through MMEC and finite element method (FEM) are compared in Figure 12 under no-load and full-load conditions. In addition to the harmonics due to the slotting effect, sixth harmonic is also clearly seen in waveform of T_e under loading condition.

4.2 | Magnetic field analysis

To calculate the air-gap magnetic field for every operating point, it is firstly necessary to calculate the distribution of scalar magnetic potential on the inner surface of stator and outer surface of rotor (U_s and U_r) [17]. These distributions are then translated into equivalent virtual currents on $r = R_s$ and $r = R_r$ as follows:
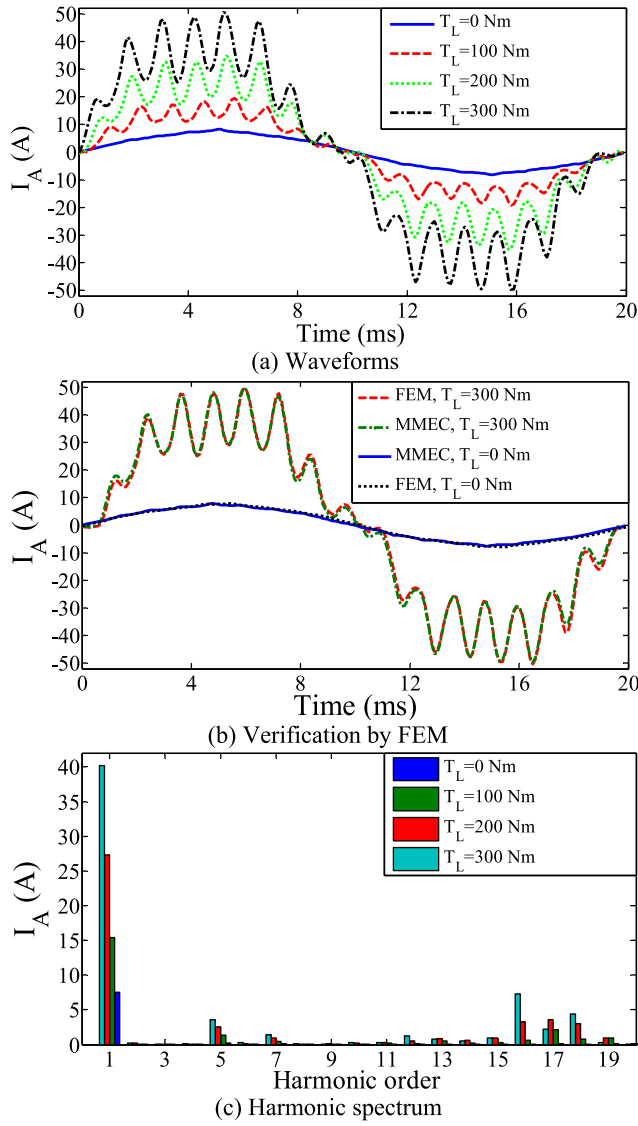
(a) Waveforms

(b) Verification by FEM

(c) Harmonic spectrum

FIGURE 10   Stator phase current.

FIGURE 11   Rotor speed.

(a) No-load condition

(b) Full-load condition ($T_L=300$ N.m)

FIGURE 12   Electromagnetic torque.

$$\begin{cases} I_{vs}(i) = U_s(i) - U_s(i+1) \\ I_{vr}(j) = U_r(j) - U_r(j+1) \end{cases} \quad (22)$$

where R_s and R_r are, respectively, the inner radius of stator and outer radius of rotor.

Consequently, the motor geometry including all ideal and non-ideal effects (MMF sources and MMF drops) is transformed into an annular domain with inner radius of R_r and outer radius of R_s which is including two distributions of equivalent virtual currents on $r = R_s$ and $r = R_r$. The approach presented in Figure 5 and Equations (3)–(11) is then used to calculate the components of air-gap flux density.

Consider an operating point under the starting condition ($t = 7$ ms), the distribution of U_s and U_r, I_{vs} and I_{vr}, and B_r and B_t is shown in Figure 13. As shown, the proposed MMEC has more accuracy than the proposed HAM in ref. [17] because the air-gap region was modelled by conventional method [6] in ref.
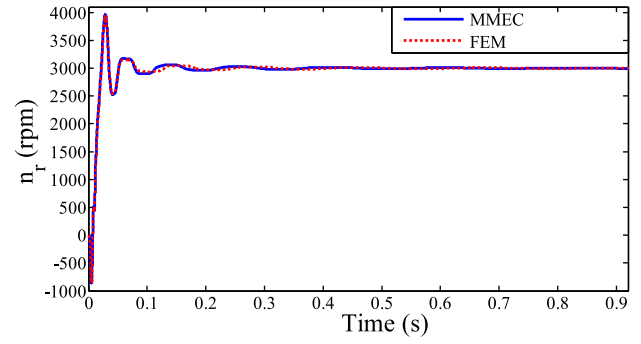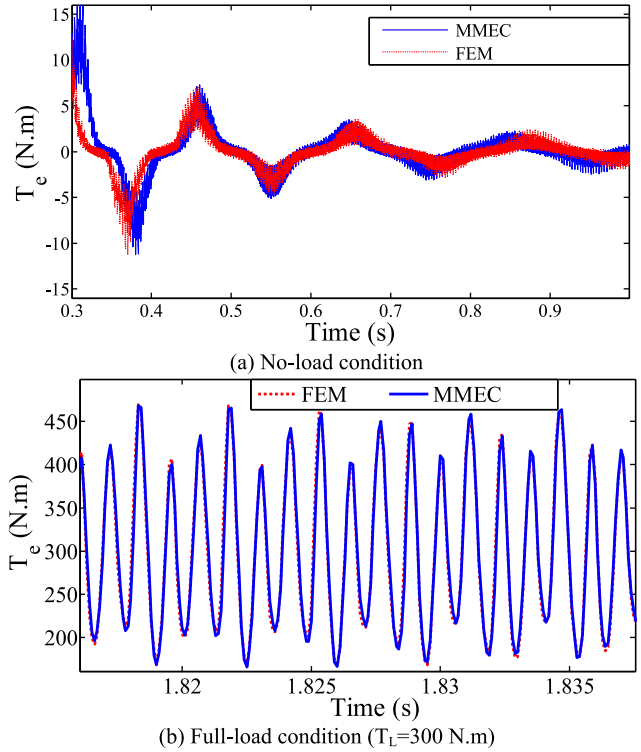
[17]. Figure 14 shows the distribution of air-gap magnetic field for a typical operating point under $T_L = 400$ N.m. As shown in Figures 13 and 14, due to the overestimation of mutual air-gap permeances by classic method [17], B_r and B_t are overestimated and underestimated by proposed HAM in ref. [17], respectively.

Figure 15 shows the 2D distribution of radial component of air-gap flux density under the starting condition. The qualitative comparison between forward and backward components of air-gap magnetic field under the starting condition obtained through 2D fast Fourier transform (FFT) is presented in Table 2.

The results of magnetic field analysis under different loading condition are presented in Table 3. The variation of
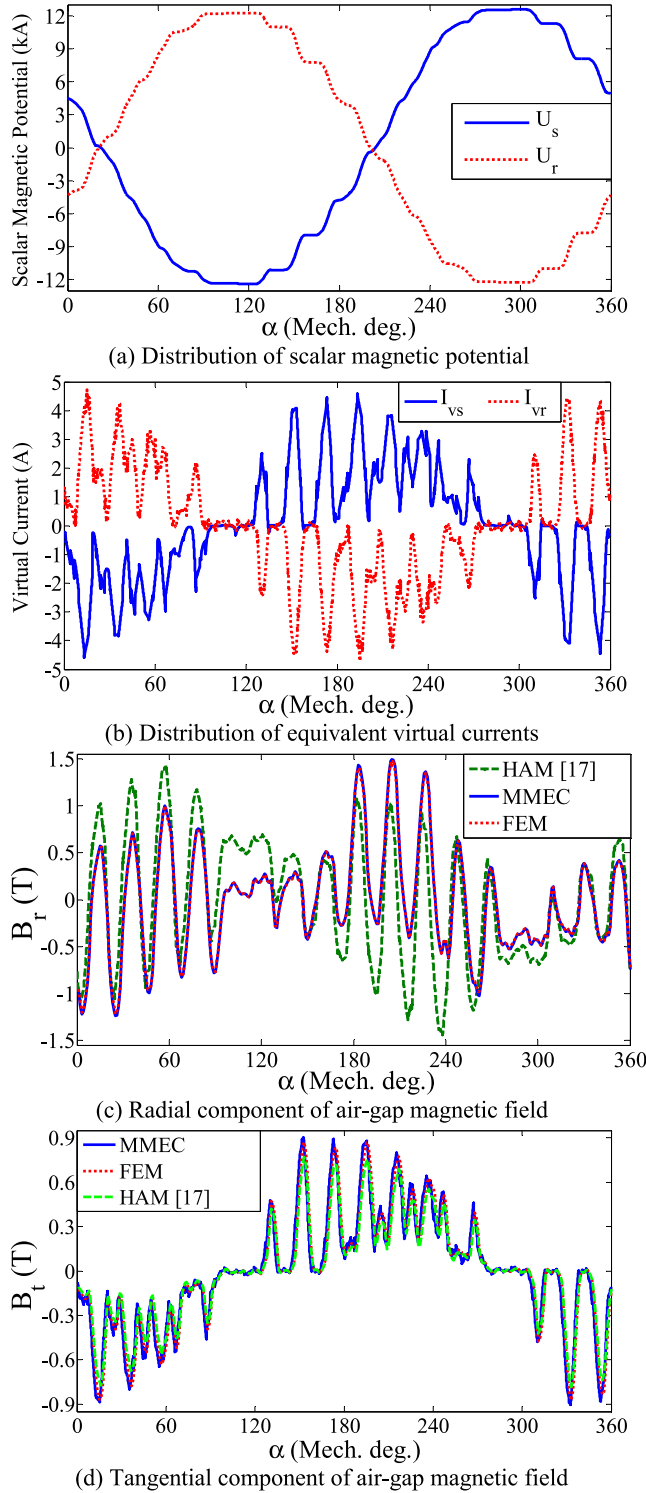
(a) Distribution of scalar magnetic potential

(b) Distribution of equivalent virtual currents

(c) Radial component of air-gap magnetic field

(d) Tangential component of air-gap magnetic field

FIGURE 13 Air-gap magnetic field under starting condition.

(a) Distribution of scalar magnetic potential

(b) Distribution of equivalent virtual currents

(c) Radial component of air-gap magnetic field

(d) Tangential component of air-gap magnetic field

FIGURE 14 Air-gap magnetic field under $T_L = 400$ N.m.

important space harmonics of B_r under different loads is shown in Figure 16. As shown, the fundamental component of B_r is reduced due to the more lagging effect of CRIMs in higher load torques.

The order of space harmonics of air-gap magnetic field due to stator and rotor slots is calculated as follows [27]:

$$\begin{cases} i = 2 \times m \times k \times q_s \pm 1 \\ j = 2 \times m \times k \times q_r \pm 1 \end{cases} \tag{23}$$

where m is the number of stator phases, k is an non-zero integer number, $q_s = \frac{N_s}{2 \times p \times m}$ and $q_r = \frac{N_r}{2 \times p \times m}$.

The results obtained through Equation (23) show the 15th harmonic is only due to the rotor slots, the 19th harmonic is

only due to the stator slots, and 17th harmonic is due to both of stator and rotor slots. As shown in Figure 16, 17th harmonic is more intensified in higher load torques.

To verify the proposed MMEC model, an experiment set-up is prepared for locked-rotor test, as shown in Figure 17. The rotor locker has been shown in zoomed view in Figure 17. The reduced voltages of 600 (V-RMS) and 690 (V-RMS) are applied to the three-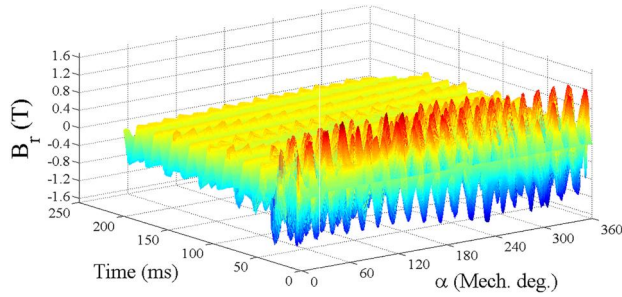phase stator winding under the locked-rotor condition. The root mean square (RMS) value of stator current obtained through MMEC model and experiment set-up are compared in Table 4. As shown, there is a good agreement between corresponding results.

5 | CONCLUSION

This paper presents an improvement in electromagnetic modelling and magnetic field analysis by MEC model. A new approach was introduced for calculating the air-gap permeances by using the CM method. The real paths of air-gap flux tubes can be well considered by proposed approach including the fringing effect in high reluctance region and concentration effect in low reluctance region. Compared to conventional MEC model, the magnetic field analysis can be done by using the MMEC model. For every operating point, the effect of MMF drop in iron parts and MMF sources of winding is replaced with two distributions of equivalent virtual currents on the inner surface of stator and outer surface of rotor. The CM method is then used to calculate the components of air-gap magnetic field. In this way, magnetic field analysis in air gap was done under starting and different loading condition, and the higher harmonic content of air-gap
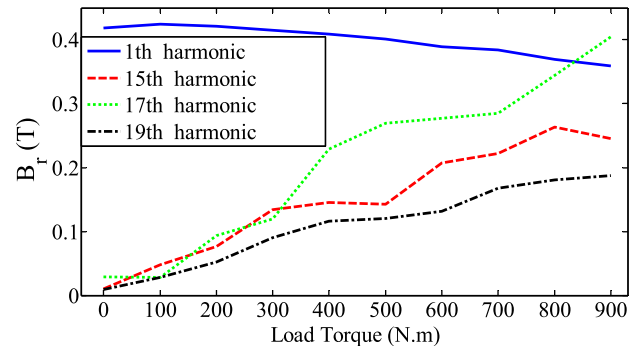

FIGURE 15 2D distribution of B_r.

TABLE 2 Forward and backward components of air-gap field.

Harmonic order	Comparison
1	$B_{1+} \ggg B_{1-}$
5	$B_{5+} < B_{5-}$
7	$B_{7+} > B_{7-}$
11	$B_{11+} < B_{11-}$
13	$B_{13+} > B_{13-}$
15	$B_{15+} > B_{15-}$
17	$B_{17+} < B_{17-}$
19	$B_{19+} > B_{19-}$

FIGURE 16 Variation of important harmonics due to loading effect.

TABLE 3 FFT spectrum of B_r under different T_L.

|	1st harmonic	5th h	7th h	11th h	13th h	15th h	17th h	19th h
$T_L = 0$ N.m	0.418	0.005	0.006	0.0017	0.0032	0.0096	0.028	0.009
$T_L = 100$ N.m	0.424	0.0096	0.017	0.019	0.014	0.0476	0.0283	0.0279
$T_L = 200$ N.m	0.421	0.0183	0.0245	0.019	0.016	0.0767	0.0938	0.0525
$T_L = 300$ N.m	0.415	0.0339	0.043	0.05	0.019	0.134	0.119	0.09
$T_L = 400$ N.m	0.409	0.0307	0.038	0.035	0.042	0.145	0.228	0.115
$T_L = 500$ N.m	0.401	0.034	0.04	0.021	0.033	0.143	0.269	0.12
$T_L = 600$ N.m	0.389	0.065	0.039	0.05	0.079	0.207	0.047	0.131
$T_L = 700$ N.m	0.383	0.064	0.063	0.058	0.029	0.222	0.284	0.167
$T_L = 800$ N.m	0.369	0.081	0.056	0.052	0.078	0.263	0.215	0.18
$T_L = 900$ N.m	0.358	0.073	0.065	0.056	0.052	0.245	0.404	0.187
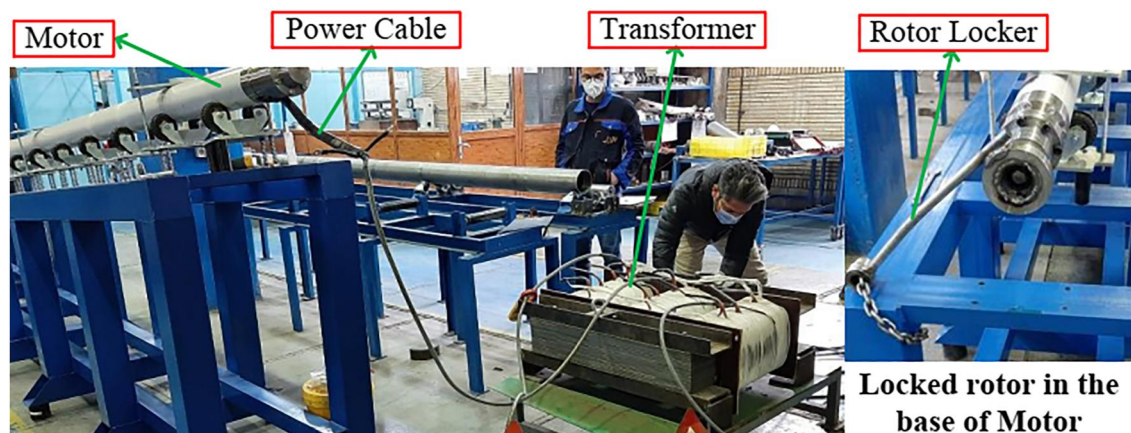
FIGURE 17 Experiment set-up.

TABLE 4 Results of locked-rotor test.

	MMEC	Experiment
$V_{L-L} = 600$ (V-RMS)	13.54 (A)	13.5 (A)
$V_{L-L} = 690$ (V-RMS)	18.07 (A)	18 (A)

magnetic field due to the loading effect was concluded. The proposed MMEC model can be used to model and for the analysis of different electric machines.

AUTHOR CONTRIBUTIONS

Farhad Rezaee-Alam: Formal analysis; Software; Validation; Writing; Writing – review and Editing. **Abbas Nazari Marashi**: Conceptualisation; formal analysis; investigation; Methodology; resources; Software; Validation; Writing – review and Editing. **Sam Roozbehani**: Conceptualisation; Investigation; Project administration; Supervision; Writing – review and editing.

ACKNOWLEDGEMENTS

CONFLICT OF INTEREST STATEMENT
The authors whose names are listed immediately above certify that they have NO affiliations with or involvement in any organisation or entity with any financial interest (such as honoraria; educational grants; participation in speakers' bureaus; membership, employment, consultancies, stock ownership, or other equity interest; and expert testimony or patent-licensing arrangements), or non-financial interest (such as personal or professional relationships, affiliations, knowledge or beliefs) in the subject matter or materials discussed in this manuscript.

DATA AVAILABILITY STATEMENT
No data are available.

ORCID
Sam Roozbehani https://orcid.org/0000-0001-9834-8838

REFERENCES

1. Sudhoff, S.D., et al.: Magnetic equivalent circuit modeling of induction motors. IEEE Trans. Energy Convers. 22(2), 259–270 (2007)
2. Asad, B., et al.: The modeling and investigation of slot skews and supply imbalance on the development of principal slotting harmonics in squirrel cage induction machines. IEEE Access 9, 165932–165946 (2021)
3. Hu, J., Liu, F., Li, Y.: An improved sub-domain model of flux switching permanent magnet machines considering harmonic analysis and slot shape. IEEE Access 9, 55260–55270 (2021)
4. Mirazimi, M.S., Kiyoumarsi, A.: Magnetic field analysis of SynRel and PMASynRel machines with hyperbolic flux barriers using conformal mapping. IEEE Trans. Transport. Electrific. 6(1), 52–61 (2020)
5. Ajily, E., Abbaszadeh, K., Ardebili, M.: Three-dimensional field reconstruction method for modeling axial flux permanent magnet machines. IEEE Trans. Energy Convers. 30(1), 199–207 (2015)
6. Ostovic, V.: Dynamics of Saturated Machines. Springer-Verlag, New York. ISBN 0387970797
7. Meshgin-Kelk, H., Milimonfared, J., Toliyat, H.A.: A comprehensive method for the calculation of inductance coefficients of cage induction machines. IEEE Trans. Energy Convers. 18(2), 187–203 (2003)
8. Naderi, P.: Modified magnetic-equivalent-circuit approach for various faults studying in saturable double-cage-induction machines. IET Elec. Power. Appl. 11(7), 1224–1234 (2017)
9. Hemeida, A., Sergeant, P.: Analytical modeling of surface PMSM using a combined solution of Maxwell's equations and magnetic equivalent circuit (MEC). IEEE Trans. Magn. 50(12) (2014)
10. Ladghem-Chikouche, B., et al.: Two-dimensional hybrid model for magnetic field calculation in electrical machines: exact subdomain technique and magnetic equivalent circuit. COMPEL 40(3), 535–560 (2021)
11. Rezaee-Alam, F., Hosseini, M., Rezaeealam, B.: A New Hybrid Analytical Model for Electromagnetic Analysis of Wound Rotor Induction Motors. Int. J. Num. Model. Electron. Netw. Dev. Fields 35(6), 1–21 (2022). (Early Access)
12. Ding, L., et al.: A novel mesh-based equivalent magnetic network for performance analysis and optimal design of permanent magnet machines. IEEE Trans. Energy Convers. 34(3), 1337–1346 (2019)
13. Saneie, H., Nasiri-Gheidari, Z.: Performance analysis of outer-rotor single-phase induction motor based on magnetic equivalent circuit (MEC). IEEE Trans. Ind. Electron. 68(2), 1046–1054 (2021)
14. Wu, L.J., et al.: On-load field prediction of surface-mounted PM machines considering nonlinearity based on hybrid field model. IEEE Trans. Magn. 55(3), 8100911 (2019)
15. Li, Z., et al.: Open-circuit field prediction of interior permanent-magnet motor using hybrid field model accounting for saturation. IEEE Trans. Magn. 55(7), 8104707 (2019)

16. Li, Z., et al.: An improved hybrid field model for calculating on-load performance of interior permanent-magnet motors. IEEE Trans. Ind. Electron. 68(10), 9207–9217 (2021)

17. Rezaee-Alam, F., et al.: Analytical odeling of one cage rotor inducton motor for electric submersible pumps. IET Elec. Power. Appl. 16(11), 1273–1285 (2022). Article in Press

18. Rezaee-Alam, F., Rezaeealam, B., Naeini, V.: An improved winding function theory for accurate modeling of small and large air-gap electric machines. IEEE Trans. Magn. 57(5), 8104513 (2021)

19. Rezaee-Alam, F., Rezaeealam, B.: An enhanced analytical technique based on winding function theory for analysis of induction motors. Int. Trans. Electr. Energy Syst. 31(5) (2021). https://doi.org/10.1002/2050-7038.12863

20. Rezaee-Alam, F., Hamidi, A., Hosseini, M.: A new hybrid analytical model based on winding function theory for analysis of unbalanced two-phase induction motors. Scientia Iranica (2022). Article in Press. https://doi.org/10.24200/sci.2022.57654.5348

21. Brinner, T.R., McCoy, R.H., Kopecky, T.: Induction versus permanent-magnet motors for electric submersible pump field and laboratory comparisons. IEEE Trans. Ind. Appl. 50(1), 174–181 (2014)

22. Takacs, G.: Electrical submersible pumps: design, operations, and maintenance. ScienceDirect (2018). https://doi.org/10.1016/C2017-0-01308-3

23. Rezaeealam, B., Rezaee-Alam, F.: A new optimal design of surface mounted permanent magnet synchronous motors with integral slot per pole. COMPEL 37(1), 136–152 (2018)

24. Abbaszadeh, K., Rezaee-Alam, F.: On-load field component separation in surface-mounted permanent-magnet motors using an improved conformal mapping method. IEEE Trans. Magn. 52(2), 5200112 (2016)

25. Rezaee-Alam, F., Abbaszadeh, K.: Magnetic field analysis in eccentric surface-mounted permanent-magnet motors using an improved conformal mapping method. IEEE Trans. Energy Convers. 31(1), 333–344 (2016)

26. Asghari, B.: Geometrical permeance network based real-time nonlinear induction machine model. PhD Thesis, University of Alberta, Edmonton (2011)

27. Boldea, I., Nasar, S.A.: The Induction Machines Design Handbook. CRC Press, Boca Raton, FL (2009)